PAPER

Check for updates

A unique sandwich structure of a CoMnP/Ni$_2$P/NiFe electrocatalyst for highly efficient overall water splitting†

Xiuming Bu,[a] Renjie Wei, [ID] [ab] Wei Gao, [ID] [c] Changyong Lan[a] and Johnny C. Ho [ID] *[abd]

Rational design of active and stable bifunctional electrocatalysts for both hydrogen evolution and oxygen evolution reactions is critical for the realization of renewable energy technologies. Although direct growth of active two-dimensional (2D) nanosheets on the current collector is an effective method to improve the exposure of active sites, the inefficient electron transfer and weak electron interaction between 2D nanosheets and current collectors greatly limit their overall electrochemical performance. Herein, a unique sandwich structure of CoMnP/Ni$_2$P/NiFe is successfully designed *via* introducing a Ni$_2$P interlayer between CoMnP nanosheets and nickel–iron (NiFe) foam to achieve an excellent bifunctional electrocatalyst in alkaline media. The metallic Ni$_2$P interlayer does not only improve the electron transfer from the current collector of NiFe foam to the catalyst of CoMnP, but also enhances the intrinsic activity of each active site *via* strong electron interaction. Electrochemical studies show that the resulting electrocatalyst exhibits superior electrocatalytic activity, such as giving a low cell voltage of only 1.48 V at 10 mA cm^{-2} stably for a long time when applied as both the cathode and anode in alkaline solutions. These results evidently indicate the superior electrochemical characteristics of this sandwich structure, which may provide a new insight into the design of electrocatalysts for different utilizations.

Introduction

Electrochemical water splitting provides a promising strategy for the conversion of water into chemicals and fuels *via* renewable electricity.[1–4] It is generally composed of two half reactions, including the cathodic hydrogen evolution reaction (HER) and anodic oxygen evolution reaction (OER), of which both are potential candidates for future sustainable clean energy supply.[5–7] However, the kinetics of the HER is sluggish in alkaline media and the OER also presents another bottleneck since it involves four proton-coupled electron transfer processes contributing a substantially large activation barrier.[8,9] Until now, Pt- and Ru/Ir-based noble materials have been widely recognized as the most efficient electrocatalysts for the HER and OER, respectively.[10–12] Unfortunately, the high-cost and scarcity of these noble metals significantly impede their practical

utilizations. At the same time, these single functional catalysts for either the OER or HER need an extra preparation process and energy input for overall water splitting, which would inevitably increase the cost in all aspects.[13,14] In order to address all these problems, extensive research has been focused on the synthesis of novel bifunctional materials, which are capable of catalyzing both the HER and OER in the same electrolyte.[15–17]

Typically, when one performs the rational design of bifunctional electrocatalysts for practical overall water splitting, two important factors must be taken into consideration.[18,19] Firstly, it is essential to increase the number of active sites, which can be achieved *via* morphology manipulation and electrode structure design. At present, the direct growth of catalysts with various morphologies (nanosheet, nanowire, nanoflower, *etc.*) on different three-dimensional (3D) conductive substrates (nickel foam, carbon fiber, *etc.*) has been demonstrated to be an effective route for improving the exposure of active sites in the electrolyte.[20,21] Secondly, it is also critical to lower the cost of catalysts without sacrificing their performance. Hence, in the past decade, there has been a great deal of efforts and progress made to replace the noble metals with earth-abundant first-row transition metals and their derivatives. Borides, carbides, nitrides, phosphides, chalcogenides and hydroxides all exhibit excellent performance towards the HER and/or OER.[22–26] Among all these, phosphides are usually explored as a bifunctional catalyst due to their high conductivity and active oxyhydroxide

[a]Department of Materials Science and Engineering, City University of Hong Kong, Kowloon, Hong Kong. E-mail: johnnyho@cityu.edu.hk

[b]Shenzhen Research Institute, City University of Hong Kong, Shenzhen 518057, P. R. China

[c]State Key Laboratory of Solidification Processing, Center for Nano Energy Materials, School of Materials Science and Engineering, Northwestern Polytechnical University and Shaanxi Joint Laboratory of Graphene (NPU), Xi'an 710072, PR China

[d]State Key Laboratory of Terahertz and Millimeter Waves, City University of Hong Kong, Kowloon, Hong Kong

† Electronic supplementary information (ESI) available. See DOI: 10.1039/c9ta02551k

This journal is © The Royal Society of Chemistry 2019

J. Mater. Chem. A, 2019, 7, 12325–12332 | 12325

surface.[27,28] For example, $Ni_2P\|Ni_2P$ catalysts were developed to facilitate the water-splitting reaction at a cell voltage of only 1.58 V in order to generate a current density of 10 mA cm^{-2}.[29] The experimental and theoretical results further proved that the synergistic effect among the multi-metal active sites could significantly optimize the corresponding reaction kinetics.[30–32] Motivated by all these above observations, we anticipate that the *in situ* growth of dual-transition-metal-phosphides on 3D substrates would generate numerous active surface species and large numbers of exposed active sites, considerably improving the overall water splitting performance. Nonetheless, these *in situ* catalysts are crudely formed on the substrate surface, while the non-intimate contact between the substrate and the active material can easily impede the charge transfer, not being active enough to drive the overall water splitting. In this regard, it is of paramount importance to achieve subtle design methods for preparing enhanced bifunctional catalysts with extensive active surface species and rapid charge transfer.

Here, we propose and develop a superior bifunctional sandwich structure of an electrocatalyst, namely $CoMnP/Ni_2P/NiFe$, toward both the HER and OER, in which the CoMnP nanosheets are prepared on hollow three-dimensional (3D) continuous nickel–iron (NiFe) foam *via* Ni_2P bonding. It is notable that the hollow 3D substrate provides a high loading capacity of CoMnP nanosheets, while the continuous low-resistance Ni_2P interlayer between the NiFe substrate and the CoMnP active material would yield an efficient electron transmission channel from the current collector to the active material. In addition, the introduction of Ni_2P can modify the electronic structure of CoMnP *via* strong electron interaction as well as enhance the contact between the active material and the substrate. Importantly, the synergistic effect of combining surface and interface engineering in this unique sandwich structure gives a remarkable OER and HER performance, which can be proved using a 1.5 V battery to power an overall water-splitting device.

Experimental

Preparation of $Ni_2P/NiFe$ foam

In this study, all the NiFe foam pieces were treated as follows: acetone treatment for 10 min, HCl treatment for 30 min, distilled water treatment for 10 min and ethanol treatment for 10 min. Ni_2P was then prepared *via* a low-temperature phosphorization process. Typically, a piece of NiFe foam (40 mm × 8 mm × 0.5 mm, $M_{Ni} : M_{Fe} = 7 : 3$) and 500 mg of NaH_2PO_2 were placed at two opposite sides of a ceramic boat with NaH_2PO_2 placed at the upstream side of a tube furnace. During the process, the system was heated to 300 °C for 2 h with a heating rate of 3 °C min^{-1} under an Ar atmosphere (flow rate = 100 sccm). After that, Ni_2P was obtained after cooling to room temperature.

Preparation of $CoMn(CO)_x(OH)_y/NiFe$ foam

In a typical process, 0.15 g of $Co(NO_3)_2 \cdot 6H_2O$, 0.12 g of $MnCl_2 \cdot 4H_2O$, 0.037 g of NH_4F and 0.18 g of urea were added into 10 mL of H_2O to form a clear solution by stirring for 15 min. Then, the mixture and a piece of NiFe foam were transferred into a 15 mL Teflon-lined stainless steel autoclave and kept at 180° for 6 h. After that, the obtained product was washed successively three times each with distilled water and ethanol, followed by drying at 60 °C for 12 h.

Preparation of $CoMn(CO)_x(OH)_y/Ni_2P/NiFe$ foam

The preparation process here is almost the same as the preparation of $CoMn(CO)_x(OH)_y$ nanosheets on NiFe foam except for replacing the NiFe foam with a piece of surface treated $Ni_2P/NiFe$ foam. The surface treatment process is divided into two steps. Firstly, $Ni_2P/NiFe$ foam was immersed into 0.2 M HNO_3 for 10 s and then washed with distilled water three times. Secondly, the sample was put into an oven at 120 °C for 5 h.

Preparation of CoMnP nanosheets on NiFe foam

CoMnP/NiFe was prepared *via* low-temperature phosphorization on the $CoMn(CO)_x(OH)_y/NiFe$ foam.

Preparation of $CoMnP/Ni_2P/NiFe$ foam

$CoMnP/Ni_2P/NiFe$ was prepared *via* low-temperature phosphorization on the $CoMn(CO)_x(OH)_y/Ni_2P/NiFe$ foam. Catalyst loading was carefully determined and found to be 2.81 mg cm^{-2}.

Materials characterization

The purity and crystalline structure of the samples were next evaluated by powder X-ray diffraction (XRD) employing a scan rate of 0.05° s^{-1} in a 2θ scan ranging from 10° to 80°, using a Bruker D2 Phaser (Bruker, Billerica, MA, USA) instrument equipped with a monochromatized Cu-Kα radiation source. The morphologies and dimensions of the samples were observed by scanning electron microscopy (SEM, Phenom Pro, Phenom-World, The Netherlands) with an accelerating voltage of 10 kV and field-emission SEM (SU-8010, Hitachi, Tokyo, Japan) with an accelerating voltage of 15 kV. Transmission electron microscopy (TEM) and high-resolution (HR) TEM were conducted using a Tecnai G^2 F30 (FEI, Hillsboro, OR, USA) with an accelerating voltage of 300 kV. X-ray photoelectron spectroscopy (XPS) was performed with a VG Multilab 2000 (Thermo Fisher Scientific, Waltham, MA, USA) photoelectron spectrometer using monochromatic Al-Kα radiation under vacuum at a pressure of 2×10^{-6} Pa. All the binding energies were referenced to the C 1s peak at 284.8 eV of the surface adventitious carbon. The molar ratio between Ni and Fe was tested *via* inductively coupled plasma atomic emission spectroscopy (PE Optima 8000, Perki-nElmer, Waltham, MA, USA).

Electrochemical measurement

For the electrochemical measurement, the active area of the electrocatalyst in contact with the electrolyte was defined by applying silicone rubber. All electrochemical characterization procedures were performed with a Gamry 300 electrochemical workstation equipped with a standard three-electrode configuration at 25 °C using a constant temperature bath. The

12326 | *J. Mater. Chem. A*, 2019, **7**, 12325–12332

This journal is © The Royal Society of Chemistry 2019

fabricated electrode sample was used as the working electrode. A saturated calomel electrode (SCE) and a carbon rod were employed as the reference electrode and counter electrode for both the HER and OER. All reported potentials were calibrated *versus* the reversible hydrogen electrode (RHE) using the equation of $E_{RHE} = E_{SCE} + (0.2415 + 0.059 \times pH)$ V, where E_{RHE} is the potential referenced to the RHE and E_{SCE} is the measured potential against the SCE reference electrode. The activities of the OER, HER and overall water splitting were surveyed in a 1 M KOH aqueous solution (pH = 13.73) by linear sweep voltammetry (LSV) at a scan rate of 5 mV s^{-1}. For comparison, commercial RuO$_2$ and Pt/C catalysts loaded on polished glassy carbon electrodes were also tested under identical conditions. In particular, using the same fabrication method, these RuO$_2$ and Pt/C electrodes were prepared by first dispersing the powders in a Nafion solution, then dropping the solutions onto the polished glassy carbon and finally drying them in the open air. The loading density of both RuO$_2$ and Pt/C powders is 0.5 mg cm^{-2}. To keep the electrode surface in a relatively stable state, 10 cyclic voltammetry (CV) cycles were operated before the assessment of OER activity until the redox peaks and the oxygen evolution currents showed no noticeable change.

Unless otherwise mentioned, the voltammograms were recorded with *iR* drop compensation automatically on the workstation. The overall water splitting stability was determined by a chronopotentiometry measurement at a current density of 10 mA cm^{-2} without any *iR* drop compensation, accordingly. The charge-transfer resistances of different samples were determined by electrochemical impedance spectroscopy (EIS) in the frequency range between 0.01 Hz and 300 kHz at with an AC voltage of 10 mV rms. Gas measurement was carried out by using gas chromatography (GC-7900, Techcomp Co.) with argon as the carrier gas. The Faraday efficiency (FE) was estimated by comparing the amount of experimentally measured hydrogen and oxygen, as well as that from the theoretical calculations using the equation It/nF, where I is the current (A), t is the duration (s), n is the number of electrons transferred, and F is the Faraday constant (96 485.338C mol^{-1}).

Results and discussion

In Fig. 1, the preparation of the CoMnP/Ni$_2$P/NiFe sandwich structure is schematically presented. In particular, NiFe foam was chosen as the substrate and served as a highly conductive current collector which is commercially available at low cost. Firstly, hollow three-dimensional NiFe foam was obtained after acid treatment due to the different reaction rates of Ni and Fe in

acid solution. After that, Ni$_2$P was *in situ* synthesized *via* low-temperature phosphorization of NiFe foam which meant that the NiFe foam was wrapped closely with the Ni$_2$P layer. The hollow Ni$_2$P/NiFe foam was then immersed into 0.2 M HNO$_3$ for 30 s and then processed with a thermal treatment at 120 °C for 5 h to obtain a hydrophilic surface. After surface treatment, CoMn(CO$_3$)$_x$(OH)$_y$ (CoMnCH) nanosheets were prepared by hydrothermally reacting Co(NO$_3$)$_2$·6H$_2$O, MnCl$_2$·4H$_2$O, and NH$_4$F with urea on the surface of Ni$_2$P/NiFe foam. Finally, the resulting CoMnCH nanosheets were converted into CoMnP nanosheets by a second phosphorization process, leading to the formation of the CoMnP/Ni$_2$P/NiFe electrocatalyst.

X-ray diffraction was first carried out to confirm the successful preparation of the CoMnP/Ni$_2$P/NiFe electrocatalyst as depicted in Fig. S1.† The XRD pattern of Ni$_2$P/NiFe foam matches well with that of the cubic Ni$_2$P (JCPDS no. 74-1385). At the same time, careful analysis of the differences in the XRD patterns of Ni$_2$P, Fe$_x$P and Ni$_x$Fe$_y$P, further confirms the coating by Ni$_2$P (rather than other phases) on NiFe foam. There are also broad peaks observed at 31.7° and 24.4° for CoMnCH, which can be attributed to the diffraction of MnCO$_3$ (JCPDS no. 83-1763) and Co(CO$_3$)$_{0.5}$(OH)·0.11H$_2$O (JCPDS no. 48-0083), respectively.[18] After phosphorization, the XRD pattern of the product can then be well indexed to CoMnP (JCPDS no. 42-0932). Notably, the characteristic peaks of Ni$_2$P are not observed in the final product of CoMnP/Ni$_2$P/NiFe which may be due to the low content of Ni$_2$P or the inner position of Ni$_2$P.

After that, the morphology of the products was also examined by scanning electron microscopy (SEM) and transmission electron microscopy (TEM). Fig. S2† exhibits a typical SEM image of 3D porous NiFe foam which has a smooth surface. The molar ratio of Ni and Fe is 7 : 3. After acid treatment, the cross-sectional SEM images of the NiFe foam can evidently prove the existence of the continuous hollow 3D NiFe foam (Fig. S3 and S4†). Fig. 2a further shows the Ni$_2$P coating on NiFe foam and the red circles indicate the hollow structure of the Ni$_2$P/NiFe hybrid. The thickness of the Ni$_2$P interlayer can be estimated to be around 100 nm from the SEM image (Fig. S5†). Importantly, there is a rough surface observed on Ni$_2$P and the corresponding energy-dispersive X-ray (EDX) elemental mapping analysis shows the uniform distribution of Ni, Fe and P (constituent elements), indicating the successful wrapping of Ni$_2$P onto the surface of NiFe foam (Fig. S6†). After HNO$_3$ and thermal treatment, there are no obvious cracks or holes observed, which suggests that the surface-coated Ni$_2$P layer is deposited as a conformal and complete structure (Fig. S7†).
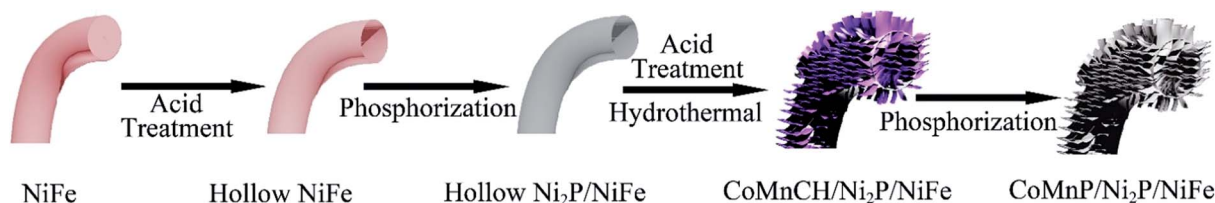

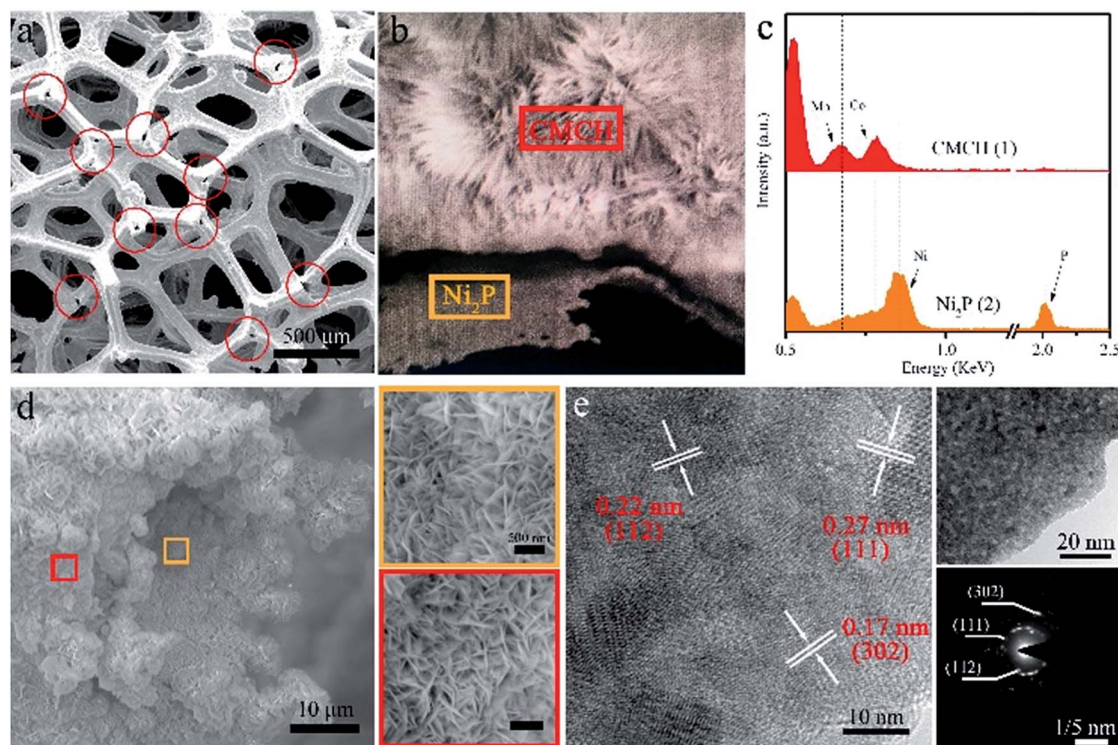**Fig. 1** The schematic illustration of the preparation process of the CoMnP/Ni$_2$P/NiFe electrocatalyst.

Fig. 2 (a) SEM image of Ni_2P after acid treatment; (b) SEM image of the cross-section of $Ni_2P/CoMnCH$ and (c) corresponding EDX profiles of the orange and red regions; (d) SEM image of $Ni_2P/CoMnP$ on NiFe foam and the magnified areas of the orange and red regions. (e) TEM image, HRTEM image and corresponding selected area electron diffraction pattern (SAED) of CoMnP nanosheets.

Meanwhile, the surface treatment enhances the intimate contact between the NiFe foam and the Ni_2P layer. Due to the transition from hydrophobicity to hydrophilicity, the sandwich structure, in which the CoMnCH nanosheets are synthesized on the Ni_2P surface, is successfully obtained as shown in Fig. 2b. The obvious elemental difference on both the nanosheets and interlayer also confirms the successful preparation of the sandwich structure here (Fig. 2c). Notably, both the inner and outer surfaces of the hollow $Ni_2P/NiFe$ are covered with vertical CoMnCH nanosheets as marked by red and orange regions, in which the active material loading can be substantially enhanced here (Fig. 2d). Also, this improved exposure of the active sites derived from the hollow structure can be an important factor for the performance improvement.[33] At the same time, it is interesting that the CoMnCH nanosheets appear only in the section which is in contact with the solution directly, since the nanosheets cannot be found in the inner space of the structure (Fig. S8 and S9†). In any case, based on the SEM image, the thickness of CoMnP is determined to be around 43 nm. Moreover, the individual CoMnP nanosheets consist of a large number of crystalline nanoparticles, which are possibly formed due to the lattice mismatch during the growth of the sandwich structure (Fig. 2e). Lots of pores are then obtained when the nanoparticles coalesce, enhancing the exposure of active sites and thus improving the electrocatalytic performance of the structure. As revealed by the HRTEM image, lattice fringes of 0.27 nm, 0.22 nm and 0.17 nm are clearly observed, which correspond to the (111), (112) and (302) planes of the as-

prepared CoMnP samples. Combined with the SAED pattern, all these findings evidently confirmed the successful preparation of CoMnP nanosheets.

Furthermore, XPS measurements were also performed to assess the chemical valence states of samples during the preparation process as well as to investigate the change in chemical states after the introduction of the Ni_2P interlayer. Fig. 3 shows the Ni 2p, O 1s and P 2p core-level XPS spectra of all samples. For the Ni 2p spectra, the main peak located at 856.59 eV can be ascribed to the oxidized Ni^{2+}/Ni^{3+} while the peak observed at 862.44 eV corresponds to the satellite peak (Fig. 3a).[34] Meanwhile, the peak located at 853.32 eV is attributed to the Ni–P bonding, which proves the presence of partially charged Ni species ($Ni^{\delta+}$).[34] In the O 1s spectra, two main peaks observed at 531.44 and 533.12 eV are related to the surface hydroxides and chemisorbed oxygen, respectively (Fig. 3b).[35] In the high-resolution P 2p spectra, the profile shows the notable features of phosphides with two characteristic peaks at 134.09 and 130.12 eV, which can be assigned to the oxidized phosphorus and reduced phosphorus in the form of phosphides ($P^{\delta-}$) (Fig. 3c).[34,36] All these results clearly indicate the successful preparation of Ni_2P onto the surface of NiFe foam. After acid and thermal treatment, the intensity of two $Ni^{\delta+}$ peaks is weakened and the binding energy is down-shifted by 0.51 eV, indicating a change in the electronic structure. This finding is also supported by the down-shift of the binding energy of the P 2p peak. Simultaneously, the peak intensity at 533.30 eV in the O 1s region increases a lot due to the improvement of
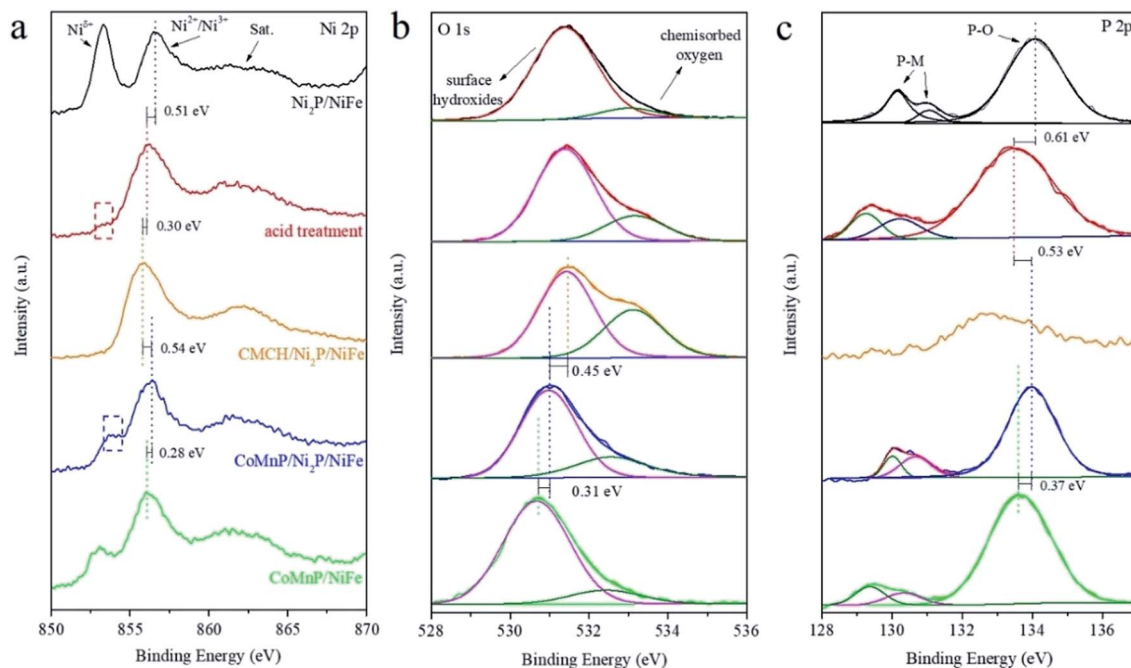
12328 | *J. Mater. Chem. A*, 2019, **7**, 12325–12332

This journal is © The Royal Society of Chemistry 2019

Fig. 3 XPS characterization of Ni_2P, acid and thermally treated Ni_2P, $CoMnCH/Ni_2P$, $CoMnP/Ni_2P$ and CoMnP on NiFe foam: (a) Ni 2p; (b) O 1s; (c) P 2p.

hydrophilicity of the samples. Therefore, the modified electronic structure and hydrophilicity enhancement may be attributed to the oxidation of the Ni_2P surface. These changes are all based on the Ni_2P phase because of the similar XPS profile of P 2p before and after acid treatment. In other words, the acid and thermal treatment did not induce any phase transformation of the Ni_2P interlayer. Subsequently, CoMnCH nanosheets were prepared via the hydrothermal method. The EDX profile and corresponding elemental mapping of the sample cross section verify the existence of the Ni_2P interlayer after thermal treatment (Fig. 2b and S10†). In this case, the nearly disappeared XPS signal of P 2p can be assigned to the deposited CoMnCH nanosheets, which attenuate the XPS signal collected from the Ni_2P interlayer. Finally, the $CoMnP/Ni_2P/NiFe$ sandwich structure was prepared via a second phosphorization process. This way, the two $Ni^{\delta+}$ peaks appear again on the final product to confirm the effectiveness of this second phosphorization. As compared with those of CoMnP/NiFe, the XPS peaks of Ni are further positively shifted (0.28 eV). The Co 2p and Mn 2p peaks also exhibit the same trend as shown in Fig. S11,† indicating that the existence of the Ni_2P interlayer offers an opportunity to generate strong electron interactions with fabricated CoMnP nanosheets, where the protons would be transferred based on the following the sequence: NiFe foam, positively charged Ni ($Ni^{\delta+}$), negatively charged P species in Ni_2P, positively charged Co and Mn, negatively charged P species in CoMnP.

To shed light on the superior electrochemical characteristics of this sandwich structure, both the HER and OER are adopted to evaluate the catalytic performance of $CoMnP/Ni_2P/NiFe$ in 1 M KOH. For comparison, a commercial noble catalyst, the

NiFe foam, the CoMnP/NiFe electrode and the $Ni_2P/NiFe$ electrode are all examined. As shown in Fig. 4a, the NiFe foam exhibits poor activity towards the OER. After phosphorization, $Ni_2P/NiFe$ exhibits good catalytic performance, requiring an overpotential of 270 mV to achieve a current density of 50 mA cm^{-2}. At the same time, the CoMnP/NiFe sample shows similar OER performance, while the required overpotential is 240 mV
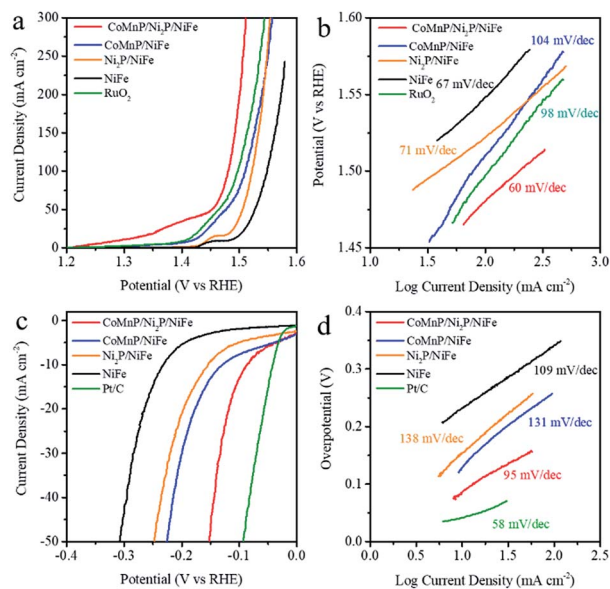

Fig. 4 (a) OER linear sweep voltammetry curves of different electrocatalysts in 1 M KOH with a scan rate of 5 mV s^{-1}; (b) Tafel plots for the OER; (c) HER linear sweep voltammetry curves of different electrocatalysts and (d) corresponding Tafel plots.

for a current density of 50 mA cm^{-2}. Also, when the Ni$_2$P interlayer is introduced between the CoMnP nanosheets and the NiFe foam, the CoMnP/Ni$_2$P/NiFe sample gives the best catalytic performance in terms of overpotentials of 204 mV, 220 mV and 250 mV at current densities of 10 mA cm^{-2}, 50 mA cm^{-2} and 100 mA cm^{-2}, respectively (Fig. S12†). The excellent OER performance is even better than that of commercial RuO$_2$ (1.49 V at 10 mA cm^{-2}). This superior OER performance is further demonstrated by its smallest Tafel slope which is derived from the LSV curves as shown in Fig. 4b. While commercial RuO$_2$, CoMnP/NiFe and Ni$_2$P/NiFe have Tafel slopes of 98 mV dec^{-1}, 71 mV dec^{-1} and 104 mV dec^{-1}, respectively, the CoMnP/Ni$_2$P/NiFe sample exhibits an impressively small Tafel slope of 60 mV dec^{-1}, which is close to the 59 mV dec^{-1} associated with one electron transferring back to the electrode before the rate-determining step. Electrochemical impendence spectroscopy (EIS) measurements are also conducted to further confirm the OER kinetics. The intercept on the Z'-axis in the plot corresponds to the electrode and electrolyte resistance (R_Ω) whereas the width of the semicircle represents the charge-transfer resistance (R_{ct}).[37] It is clear that CoMnP/Ni$_2$P/NiFe has the lowest R_Ω and R_{ct} among all the samples, which indicates the fastest OER kinetics (Fig. S13†). In addition, in order to evaluate the electrochemically active surface area (ECSA) of these electrodes, the double layer capacitance (C_{dl}) is measured from −0.25 to −0.2 V with scan rates of 100, 150, 200 and 250 mV s^{-1}. It can be observed that CoMnP/Ni$_2$P/NiFe has the highest C_{dl} of 5 mF cm^{-2}, followed by CoMnP/NiFe (4 mF cm^{-2}) and Ni$_2$P/NiFe (2.8 mF cm^{-2}) (Fig. S14†). This C_{dl} improvement evidently demonstrates the favorable effect of the Ni$_2$P interlayer on the electronic structure of the outer CoMnP surface.

In addition, the electrocatalytic HER performance of all these samples is also assessed in 1 M KOH. Fig. 4c displays the polarization curves obtained from linear sweep voltammetry at a scan rate of 5 mV s^{-1}. It is witnessed that CoMnP/Ni$_2$P/NiFe exhibits overpotentials of 87 and 150 mV to afford the current densities of 10 and 50 mA cm^{-2}, respectively. At the same current density of 10 mA cm^{-2}, the Pt/C, CoMnP/NiFe, Ni$_2$P/NiFe and NiFe electrodes require overpotentials of 42 mV, 129 mV, 154 mV and 232 mV, respectively. The Tafel plots derived from HER polarization curves with iR correction further prove that the introduction of the Ni$_2$P layer results in the CoMnP/Ni$_2$P/NiFe catalyst having the lowest Tafel slope (95 mV dec^{-1}) among all the samples here except for the commercial Pt/C electrode (Fig. 4d). Importantly, the polarization curves of CoMnP/Ni$_2$P/NiFe for both the OER and HER are obtained for 1000 cycles in 1 M KOH, in which there is no obvious change, suggesting the insignificant degradation of current densities during long-term cycling (Fig. S15†).

It is well established that both the increasing number and the modified electronic structure of active sites are the main factors contributing to the excellent HER and OER performance of the electrocatalyst. The enlarged surface area provided by the hollow structure of NiFe foam can improve the coverage of the Ni$_2$P interlayer and the exposure of electrochemically active sites of CoMnP nanosheets. For the composite CoMnP/Ni$_2$P/

NiFe foam, the metallic behavior of Ni$_2$P can then further facilitate the modification of the electronic structure of active sites of nanosheets as observed in XPS analysis where the positively shifted binding energies of Co and Mn clearly suggest the existence of Ni$_2$P inducing the stronger electronic interaction with the interlayer here. Moreover, the lowest electrolyte resistance and the charge transfer resistance of the sandwich structure can also indicate the efficient charge transport ability of the composite via the bonding between CoMnP nanosheets and NiFe substrates, which substantially enhances the overall electrochemical activity of the structure towards both the HER and OER.

Due to the excellent electrocatalytic performance of CoMnP/Ni$_2$P/NiFe for both the OER and HER, this sandwich structured electrode can be perfectly used as a bifunctional catalyst for overall water splitting in a 1 M KOH solution. As illustrated in Fig. 5a, the CoMnP/Ni$_2$P/NiFe catalyst requires only a 1.48 V cell potential to generate a current density of 10 mA cm^{-2}, indicating that our catalyst can serve as an earth-abundant and impressive bifunctional electrocatalyst here. At the same time, vigorous oxygen and hydrogen bubbling can also be observed clearly when the two-electrode overall water splitting system is powered with a 1.5 V battery (Fig. 5b and Video S1†). The faradaic efficiency (FE) for overall water splitting was calculated by comparing the amounts of experimentally obtained H$_2$ and O$_2$ with the theoretically calculated ones (Fig. S16†). The agreement between both values indicates that the FE is nearly 100%, with the molar ratio of H$_2$ and O$_2$ being close to 2 : 1. Notably, the long-term electrochemical stability of CoMnP/Ni$_2$P/NiFe is
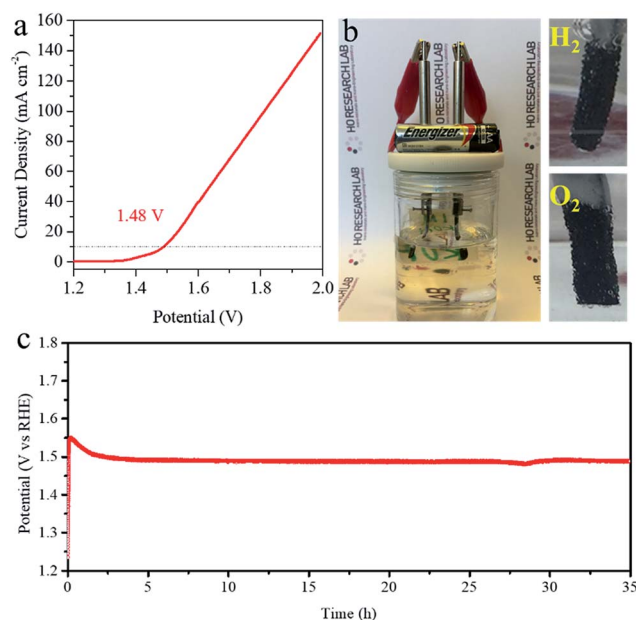

Fig. 5 (a) LSV curves of overall water splitting in a two-electrode configuration. The position of the dashed line is at 10 mA cm^{-2}. (b) Digital photo of the overall water splitting setup driven by a 1.5 V battery. The top right and bottom right images are H$_2$ and O$_2$, respectively. (c) The stability of the water splitting process at a current density of 10 mA cm^{-2} for 35 h.

also investigated for the full water splitting. It is evident that a cell potential of ~1.5 V only is required for the process, while the generated current density of 10 mA cm^{-2} can be stabilized for at least 35 h, in which this overpotential is much smaller than that of most of the non-noble metal based bifunctional catalysts for overall water splitting (Table S1†). Moreover, after the long-term stability test, the catalyst still maintains the sandwich structure as compared with the original catalyst where only small areas of cracks are observed (Fig. S17†).

Conclusions

In summary, we have successfully prepared a novel sandwich structure containing CoMnP nanosheets and 3D hollow NiFe foam which are interconnected with Ni$_2$P bonding. Importantly, the obtained CoMnP/Ni$_2$P/NiFe exhibits extremely excellent electrocatalytic performance and stability towards the HER, OER and overall water splitting. The high bifunctional activity is mainly attributed to the structural design, interface and surface engineering: (1) 3D hollow NiFe foam provides enough loading capacity for CoMnP nanosheets, which enhance the exposure of active sites; (2) the Ni$_2$P sublayer between CoMnP and NiFe foam provides rapid electron pathways to increase the electron transfer; (3) the electronic structure of active sites on CoMnP nanosheets is modified by Ni$_2$P *via* strong electron interaction thus improving the intrinsic activity of surface active species. We believe that this unique sandwich structure design would provide a new insight into electrocatalyst applications, being generally adoptable for other catalytic applications based on transition-metal-based compounds.

Conflicts of interest

There are no conflicts to declare.

Acknowledgements

References

1 X. Zou and Y. Zhang, *Chem. Soc. Rev.*, 2015, **44**, 5148–5180.

2 M. Fang, G. Dong, R. Wei and J. C. Ho, *Adv. Energy Mater.*, 2017, **7**, 1700559.

3 A. Tiwari, T. Novak, X. Bu, J. Ho and S. Jeon, *Catalysts*, 2018, **8**, 551.

4 N.-T. Suen, S.-F. Hung, Q. Quan, N. Zhang, Y.-J. Xu and H. M. Chen, *Chem. Soc. Rev.*, 2017, **46**, 337–365.

5 J. Nai and X. W. D. Lou, *Adv. Mater.*, 2018, 1706825.

6 J. D. Wiensch, J. John, J. M. Velazquez, D. A. Torelli, A. P. Pieterick, M. T. McDowell, K. Sun, X. Zhao, B. S. Brunschwig and N. S. Lewis, *ACS Energy Lett.*, 2017, **2**, 2234–2238.

7 M. Yu, S. Zhao, H. Feng, L. Hu, X. Zhang, Y. Zeng, Y. Tong and X. Lu, *ACS Energy Lett.*, 2017, **2**, 1862–1868.

8 J. Xiong, J. Li, J. Shi, X. Zhang, N. T. Suen, Z. Liu, Y. Huang, G. Xu, W. Cai, X. Lei, L. Feng, Z. Yang, L. Huang and H. Cheng, *ACS Energy Lett.*, 2018, **3**, 341–348.

9 Q. He, H. Xie, Z. U. Rehman, C. Wang, P. Wan, H. Jiang, W. Chu and L. Song, *ACS Energy Lett.*, 2018, **3**, 861–868.

10 Y. Pi, N. Zhang, S. Guo, J. Guo and X. Huang, *Nano Lett.*, 2016, **16**, 4424–4430.

11 X. Kong, K. Xu, C. Zhang, J. Dai, S. Norooz Oliaee, L. Li, X. Zeng, C. Wu and Z. Peng, *ACS Catal.*, 2016, **6**, 1487–1492.

12 Z. J. Chen, G. X. Cao, L. Y. Gan, H. Dai, N. Xu, M. J. Zang, H. Bin Dai, H. Wu and P. Wang, *ACS Catal.*, 2018, **8**, 8866–8872.

13 R. Wei, M. Fang, G. Dong, C. Lan, L. Shu, H. Zhang, X. Bu and J. C. Ho, *ACS Appl. Mater. Interfaces*, 2018, **10**, 7079–7086.

14 H. Xia, Z. Huang, C. Lv and C. Zhang, *ACS Catal.*, 2017, **7**, 8205–8213.

15 P. W. Menezes, C. Panda, S. Loos, F. Bunschei-Bruns, C. Walter, M. Schwarze, X. Deng, H. Dau and M. Driess, *Energy Environ. Sci.*, 2018, **11**, 1287–1298.

16 X. Long, H. Lin, D. Zhou, Y. An and S. Yang, *ACS Energy Lett.*, 2018, **3**, 290–296.

17 J. Zhang, L. Qu, G. Shi, J. Liu, J. Chen and L. Dai, *Angew. Chem., Int. Ed.*, 2016, **55**, 2230–2234.

18 T. Tang, W. J. Jiang, S. Niu, N. Liu, H. Luo, Y. Y. Chen, S. F. Jin, F. Gao, L. J. Wan and J. S. Hu, *J. Am. Chem. Soc.*, 2017, **139**, 8320–8328.

19 Z. W. Seh, J. Kibsgaard, C. F. Dickens, I. Chorkendorff, J. K. Nørskov and T. F. Jaramillo, *Science*, 2017, **355**, eaad4998.

20 X. Lu and C. Zhao, *Nat. Commun.*, 2015, **6**, 1–7.

21 N. Han, K. R. Yang, Z. Lu, Y. Li, W. Xu, T. Gao, Z. Cai, Y. Zhang, V. S. Batista, W. Liu and X. Sun, *Nat. Commun.*, 2018, **9**, 1–10.

22 X. Liang, R. Dong, D. Li, X. Bu, F. Li, L. Shu, R. Wei and J. C. Ho, *ChemCatChem*, 2018, **10**, 4555–4561.

23 T. Huang, Y. Chen and J. M. Lee, *Small*, 2017, **13**, 1–8.

24 I. S. Amiinu, Z. Pu, X. Liu, K. A. Owusu, H. G. R. Monestel, F. O. Boakye, H. Zhang and S. Mu, *Adv. Funct. Mater.*, 2017, **27**, 1–11.

25 W. Zhou, X. Cao, Z. Zeng, W. Shi, Y. Zhu, Q. Yan, H. Liu, J. Wang and H. Zhang, *Energy Environ. Sci.*, 2013, **6**, 2216–2221.

26 J. S. Chen, J. Ren, M. Shalom, T. Fellinger and M. Antonietti, *ACS Appl. Mater. Interfaces*, 2016, **8**, 5509–5516.

27 M. Ledendecker, S. Krick Calderón, C. Papp, H.-P. Steinrück, M. Antonietti and M. Shalom, *Angew. Chem., Int. Ed. Engl.*, 2015, **54**, 12361–12365.

28 X. Wang, Y. V. Kolen'Ko, X. Q. Bao, K. Kovnir and L. Liu, *Angew. Chem., Int. Ed.*, 2015, **54**, 8188–8192.

This journal is © The Royal Society of Chemistry 2019

J. Mater. Chem. A, 2019, **7**, 12325–12332 | **12331**

29 P. W. Menezes, A. Indra, C. Das, C. Walter, C. Göbel, V. Gutkin, D. Schmeißer and M. Driess, *ACS Catal.*, 2017, **7**, 103–109.

30 S. Gupta, S. Zhao, X. X. Wang, S. Hwang, S. Karakalos, S. V. Devaguptapu, S. Mukherjee, D. Su, H. Xu and G. Wu, *ACS Catal.*, 2017, **7**, 8386–8393.

31 B. Zhang, X. Zheng, O. Voznyy, R. Comin, M. Bajdich, M. García-Melchor, L. Han, J. Xu, M. Liu, L. Zheng, F. P. G. De Arquer, C. T. Dinh, F. Fan, M. Yuan, E. Yassitepe, N. Chen, T. Regier, P. Liu, Y. Li, P. De Luna, A. Janmohamed, H. L. Xin, H. Yang, A. Vojvodic and E. H. Sargent, *Science*, 2016, **352**, 333–337.

32 M. Kuang, Q. Wang, H. Ge, P. Han, Z. Gu, A. M. Al-Enizi and G. Zheng, *ACS Energy Lett.*, 2017, **2**, 2498–2505.

33 Y. Dou, L. Zhang, J. Xu, C. T. He, X. Xu, Z. Sun, T. Liao, B. Nagy, P. Liu and S. X. Dou, *ACS Nano*, 2018, **12**, 1878–1886.

34 H. Liang, A. N. Gandi, C. Xia, M. N. Hedhili, D. H. Anjum, U. Schwingenschlögl and H. N. Alshareef, *ACS Energy Lett.*, 2017, **2**, 1035–1042.

35 J. X. Feng, L. X. Ding, S. H. Ye, X. J. He, H. Xu, Y. X. Tong and G. R. Li, *Adv. Mater.*, 2015, **27**, 7051–7057.

36 P. F. Liu, X. Li, S. Yang, M. Y. Zu, P. Liu, B. Zhang, L. R. Zheng, H. Zhao and H. G. Yang, *ACS Energy Lett.*, 2017, **2**, 2257–2263.

37 P. Kuang, T. Tong, K. Fan and J. Yu, *ACS Catal.*, 2017, **7**, 6179–6187.